

PAPER • OPEN ACCESS

Three-dimensional modeling of flow characteristics and the influence of non-hydrostatic pressure in a 193° sharp open channel bend

To cite this article: Y Xing *et al* 2018 *IOP Conf. Ser.: Earth Environ. Sci.* **191** 012077

View the [article online](#) for updates and enhancements.

You may also like

- [A three-dimensional non-hydrostatic mathematical model with mixed triangle and quadrilateral grids](#)
G N Yu, B Lv and Y Xing
- [Modeling shallow water waves](#)
D Lannes
- [Unreacted equation of states of typical energetic materials under static compression: A review](#)
Zhaoyang Zheng, , Jijun Zhao et al.



ECS
The
Electrochemical
Society
Advancing solid state &
electrochemical science & technology

DISCOVER
how sustainability
intersects with
electrochemistry & solid
state science research

Three-dimensional modeling of flow characteristics and the influence of non-hydrostatic pressure in a 193° sharp open channel bend

Y Xing^{1,2}, D L Zhao¹, D G Ma¹ and W D Gan¹

¹Key Laboratory of Engineering Sediment of Ministry of Transport, Tianjin Research Institute for Water Transport Engineering, Tianjin 300456, China

E-mail: xingyan3610@163.com

Abstract. A numerical model of three-dimensional free surface flows has been developed to simulate the flow pattern and bed shear stress in a sharp channel bend with 193° curved reach. The numerical model solved 3D Reynolds-averaged Navier-Stokes equations with standard $k - \epsilon$ turbulence model to compute the flow field and the finite-volume method were used as the discretization scheme. The governing equations were solved by employed the explicit projection method with two steps. The numerical predictions were verified with experiment results and showed that the model enables to resolve the complex three-dimensional flow problems and capture the main flow features in sharp channel bends. The influence of non-hydrostatic pressure was revealed by the results with and without hydrostatic pressure assumption. It concluded that the non-hydrostatic model almost has no noticeable influence on flow pattern in this sharp channel bend with highly three-dimensional flow characteristics.

1. Introduction

River meandering pattern is the normal feature of natural rivers, and straight rivers are the exception while meandering rivers are the rule. An outstanding characteristics of flow in an open channel bend is a transverse circulation (also known as secondary flows, spiral flows or helical flows), which is perpendicular to the primary flow direction, caused by the action of the centrifugal forces present in the curved channel. The magnitude and direction of the velocity and bed shear stresses are altered by the spiral flows, and then the sediment transport is also redistributed along the bend [1].

Consequently, this process is important in natural streams with respect to sediment transport, the bathymetry evolution, mixing and spreading of pollutants, heat, oxygen, nutrients and biological species, and even the conveyance capacity [2].

Since the streamwise velocity component varies from the maximum value near the free surface to zero at the riverbed, thus, the centrifugal forces push water radially outward which results in the super elevation of the free surface between the inner and the outer banks. The imbalance of the centrifugal forces and the radial pressure gradient due to water surface deformation. And the water in the upper part of the bend is drove toward the outer bank, while water close to the riverbed is migrated toward the inner bank. Accordingly, the secondary circulation is formed at the cross-section in the bend. The secondary flows combine with the main flow to produce the spiral motion, which is typical three-dimensional flow. The helical motion of water cannot be ignored in the sediment transport, riverbed shear stress distribution and even the riverbed deformation, especially in high curvature bends.



It is important and challenging to predict and understand of the 3D flow characteristics in the river bends in river engineering and management. It not only contributes to a better understanding of the three-dimensional flow characteristics, but also can provide basic flow field data for the following mass transport and bathymetry changes researches.

Abundant studies of flow or bed deformation in curved bends of different cross sections and different curvature degree with fixed or movable bed were performed by means of field observation, laboratory experiments [3-9] and two-dimensional numerical modeling [5,10-16].

Over the years many 3D numerical models of flow in open channel bends have been published [17-22]. The 3D models can describe much more comprehensive flow field conditions, especially, the detail profiles of flow field over water depth. Moreover, the 3D models can accurately simulate the helical motion directly in bends without extra semi-empirical sub-models.

Only Zeng' simulation, of the aforementioned three-dimensional models, validated and evaluated comprehensively the profiles of the streamwise velocity, the cross-section circulation, and the turbulent kinetic energy employing a non-hydrostatic three-dimensional numerical model. The simulation was executed in a sharply curved bend, which was more severe than all channel bend experiments of prior, and provided high-quality three-dimensional experiment data through high-tech measuring instrument. However, rigid lid approximation was used in the simulation. In addition, the effectiveness of the non-hydrostatic model comparing with the hydrostatic model was not much concerned, and the influence of the non-hydrostatic pressure on the flow pattern was not illustrated in such a sharply curved bends with strong secondary flow and complex helical motion [23].

The present paper focuses on the three-dimensional characteristics in a strongly curved channel flume. Firstly, in such a sharply curved bend with strong secondary flow and complex helical motion, whether the model enables to resolve the complex three-dimensional flow problems and capture the main flow features. Secondly, because the non-hydrostatic model based on the premise that the ratio of the vertical to horizontal scales of motion is not sufficiently small, like as short waves where the vertical acceleration motion is so significant that the hydrostatic approximation is not valid. The non-hydrostatic model has showed its significant benefits in short wave problems [24,25]. Comparing with that of short wave problem in ocean, the long wave problem in river channel, where the vertical motion close to the inner and outer bank is dramatic due to the helical motion of water in the transverse direction, whether this outstanding vertical motion can be captured accurately only by employing hydrostatic model, and whether the influence of non-hydrostatic need to be taken into account. So, a three-dimensional free surface model was used to reproduce the forms of water surface level and vertical velocity profiles as well as secondary flows at typical cross sections and their evolutions along the channel bend. Moreover, the influence of non-hydrostatic pressure on flow pattern in such curved channel was also considered to distinguish between the hydrostatic pressure and non-hydrostatic pressure.

The rest of the paper is organized as follows: after a description of the numerical model we applied in Section 2, the experimental description and simulation setup are presented in Section 3, in Section 4, the water surface profiles, flow field and bed shear stress as well as their mechanisms of evolution in sharp channel bends are demonstrated and analyzed, and then the obtained results are summarized in Section 5.

2. Model description

2.1. The governing equations

The 3D Reynolds-averaged Navier-Stokes equations were solved in the numerical model, and the finite-volume approach was employed as the discretization scheme. For more details about the model can be found in reference [26].

$$\frac{\partial u}{\partial x} + \frac{\partial v}{\partial y} + \frac{\partial w}{\partial z} = 0 \quad (1)$$

$$\frac{\partial u}{\partial t} + \frac{\partial u^2}{\partial x} + \frac{\partial uv}{\partial y} + \frac{\partial uw}{\partial z} = -\frac{1}{\rho} \frac{\partial p}{\partial x} + \mu_h \left(\frac{\partial^2 u}{\partial x^2} + \frac{\partial^2 u}{\partial y^2} \right) + \mu_v \frac{\partial^2 u}{\partial z^2} \quad (2)$$

$$\frac{\partial v}{\partial t} + \frac{\partial uv}{\partial x} + \frac{\partial v^2}{\partial y} + \frac{\partial vw}{\partial z} = -\frac{1}{\rho} \frac{\partial p}{\partial y} + \mu_h \left(\frac{\partial^2 v}{\partial x^2} + \frac{\partial^2 v}{\partial y^2} \right) + \mu_v \frac{\partial^2 v}{\partial z^2} \quad (3)$$

$$\frac{\partial w}{\partial t} + \frac{\partial uw}{\partial x} + \frac{\partial vw}{\partial y} + \frac{\partial w^2}{\partial z} = -g - \frac{1}{\rho} \frac{\partial p}{\partial z} + \mu_h \left(\frac{\partial^2 w}{\partial x^2} + \frac{\partial^2 w}{\partial y^2} \right) + \mu_v \frac{\partial^2 w}{\partial z^2} \quad (4)$$

where u , v and w are the velocity components in the horizontal x , y and vertical z directions, respectively; t is the time; p is the pressure; μ_h and μ_v are the coefficients of horizontal and vertical kinematic eddy viscosities, respectively; ρ is the constant water density; and g is the gravitational acceleration.

The pressure p in equations can be decomposed into the sum of its hydrostatic and a non-hydrostatic component. Thus, p can be expressed as

$$p(x, y, z, t) = p_a(x, y, t) + \rho g [\eta(x, y, t) - z] + q(x, y, z, t) \quad (5)$$

where p_a is the atmospheric pressure; the second term on the right-hand side of the equation (5) represents the barotropic contributions to the hydrostatic pressure and q denotes the non-hydrostatic pressure component.

The height function method [27] was used to capture the free surface motions with relatively high computational efficiency, especially, in large-scale problems.

At the moving free surface η , the kinematic boundary condition is

$$w|_{z=\eta} = \frac{\partial \eta}{\partial t} + u \frac{\partial \eta}{\partial x} + v \frac{\partial \eta}{\partial y} \quad (6)$$

At the riverbed bottom $z = h(x, y)$, the kinematic boundary condition is

$$w|_{z=-h} = -u \frac{\partial h}{\partial x} - v \frac{\partial h}{\partial y} \quad (7)$$

By applying Leibniz rule with kinematic boundary conditions (6) and (7), the free surface equation can be achieved by integrated continuity equation (1) over water depth:

$$\frac{\partial \eta}{\partial t} + \frac{\partial}{\partial x} \int_{-h}^{\eta} u dz + \frac{\partial}{\partial y} \int_{-h}^{\eta} v dz = 0 \quad (8)$$

In this study, the standard $k - \varepsilon$ turbulence closure model was employed to compute the diffusion coefficients. The eddy viscosity in the standard $k - \varepsilon$ model can be given by

$$\mu_t = C_\mu \frac{k^2}{\varepsilon} \quad (9)$$

where μ_t is the eddy viscosity; k is the turbulence kinetic energy; and ε is the dissipation rate.

k and ε can be described as

$$\frac{\partial k}{\partial t} + \text{div}(k\bar{U}) = \text{div} \left(\left[\nu + \frac{\mu_t}{\sigma_k} \right] \text{grad} k \right) + \mu_t G - \varepsilon \quad (10)$$

$$\frac{\partial \varepsilon}{\partial t} + \text{div}(\varepsilon \vec{U}) = \text{div} \left(\left[\nu + \frac{\mu_t}{\sigma_\varepsilon} \right] \text{grad} \varepsilon \right) + C_1 \mu_t G \frac{\varepsilon}{k} - C_2 \frac{\varepsilon^2}{k} \quad (11)$$

where G is the turbulence production term

$$G = 2 \left(\left[\frac{\partial u}{\partial x} \right]^2 + \left[\frac{\partial v}{\partial y} \right]^2 + \left[\frac{\partial w}{\partial z} \right]^2 \right) + \left(\frac{\partial u}{\partial y} + \frac{\partial v}{\partial x} \right)^2 + \left(\frac{\partial u}{\partial z} + \frac{\partial w}{\partial x} \right)^2 + \left(\frac{\partial v}{\partial z} + \frac{\partial w}{\partial y} \right)^2 \quad (12)$$

where $c_\mu=0.09$, $C_1=1.44$, $C_2=1.92$, $\sigma_k=1.0$ and $\sigma_\varepsilon=1.3$ [28].

2.2. The boundary conditions

Four boundary conditions need to be specified in channel bed simulation, including inflow, outflow, free surface and bottom. The cells at the free surface and bottom require special treatment. The standard wall functions were employed within the near wall area ($30 < D_n V_* / \nu < 100$), where D_n is the normal distance from the bed [29].

At the free surface

$$\partial k / \partial z = 0 \quad (13)$$

$$\varepsilon = (k \sqrt{c_\mu})^{1.5} / (0.07 \kappa h) \quad (14)$$

where, κ is the von Karman constant, having a universal value of 0.41 [28].

At the bottom

$$k = \frac{V_*^2}{\sqrt{c_\mu}} \quad (15)$$

$$\varepsilon = \frac{|V_*|^3}{\kappa D_n} \quad (16)$$

where V_* is the shear velocity at the bottom, it was defined by

$$V_* = \frac{V_\tau}{(1/\kappa) \ln C} \quad (17)$$

where V_τ is the velocity along to the wall.

$$C = \begin{cases} \frac{30.0}{k_s} D_n & \text{Rough bed} \\ \frac{9.05 V_* D_n}{\nu} & \text{Smooth bed} \end{cases} \quad (18)$$

At the inflow boundary, the velocity and turbulence variables were specified. In general, homogeneous turbulence can be specified simply as

$$u = \text{constant}, \quad v = 0, \quad w = 0 \quad (19)$$

$$k = 0.03 u^2 \quad (20)$$

$$\varepsilon = c_\mu \frac{k^{1.5}}{0.09h} \tag{21}$$

For open channel flow, it can be specified as

$$\frac{u}{V_*} = \begin{cases} \frac{1}{\kappa} \ln\left(\frac{30.0(z-z_0)}{k_s}\right) & \text{Rough bed} \\ \frac{1}{\kappa} \ln\left(\frac{9.05V_*(z-z_0)}{\nu}\right) & \text{Smooth bed} \end{cases} \tag{22}$$

$$v = 0, w = 0 \tag{23}$$

$$k = \frac{V_*^2}{c_\mu^{0.5}} \left(1 - \frac{z}{h}\right) \tag{24}$$

$$\varepsilon = \frac{|V_*|^3}{\kappa z} \left(1 - \frac{z}{h}\right) \tag{25}$$

At the outflow boundary, η and zero normal gradients were specified.

2.3. The numerical method

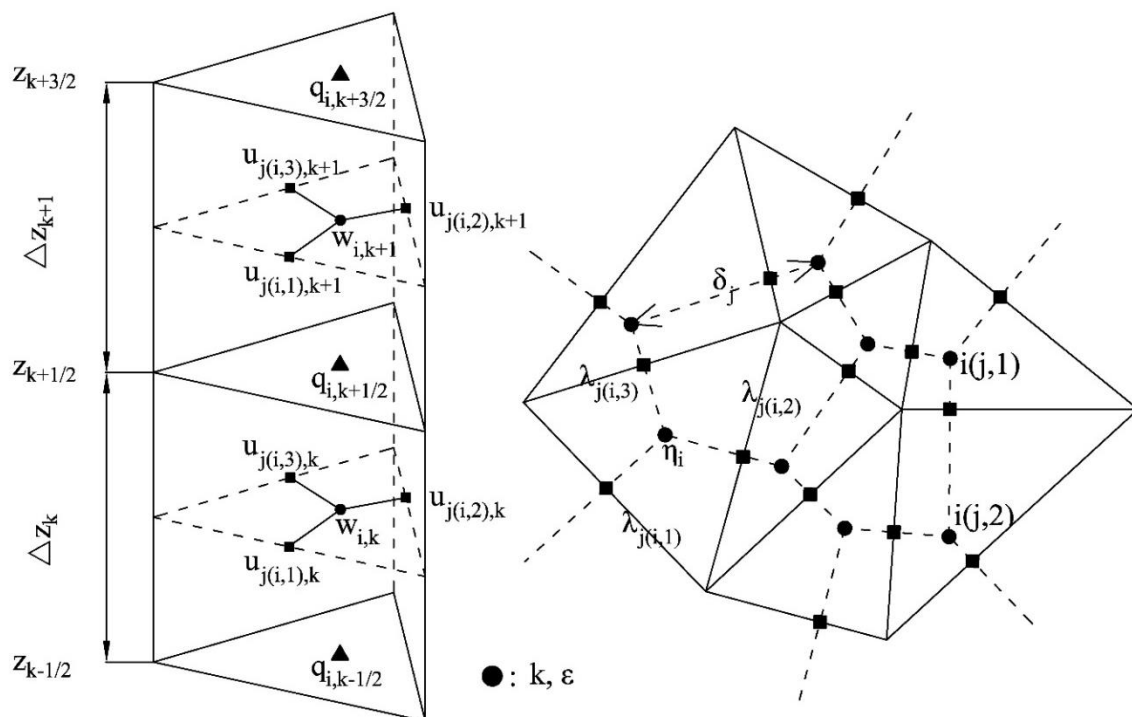


Figure 1. Grids and variables arrangement.

A boundary-fitted coordinate system in vertical direction was employed in this model. The horizontal domain was covered by a set of orthogonal unstructured grid, and the 3D numerical mesh was built with several horizontal orthogonal unstructured grid over water depth. Its advantage and challenge are

equivalent to the method based on sigma-coordinate system. If the layer thickness is defined uniformly over the water depth, the vertical coordinate system is very similar to the usual sigma-coordinate system [29].

A different variables arrangement was presented in this mesh system, which caused the PPE (Pressure Poisson Equation) was symmetric and positive definite, and then can be solved effectively [30]. The 3D grid system and variables arrangement can be founded in figure 1.

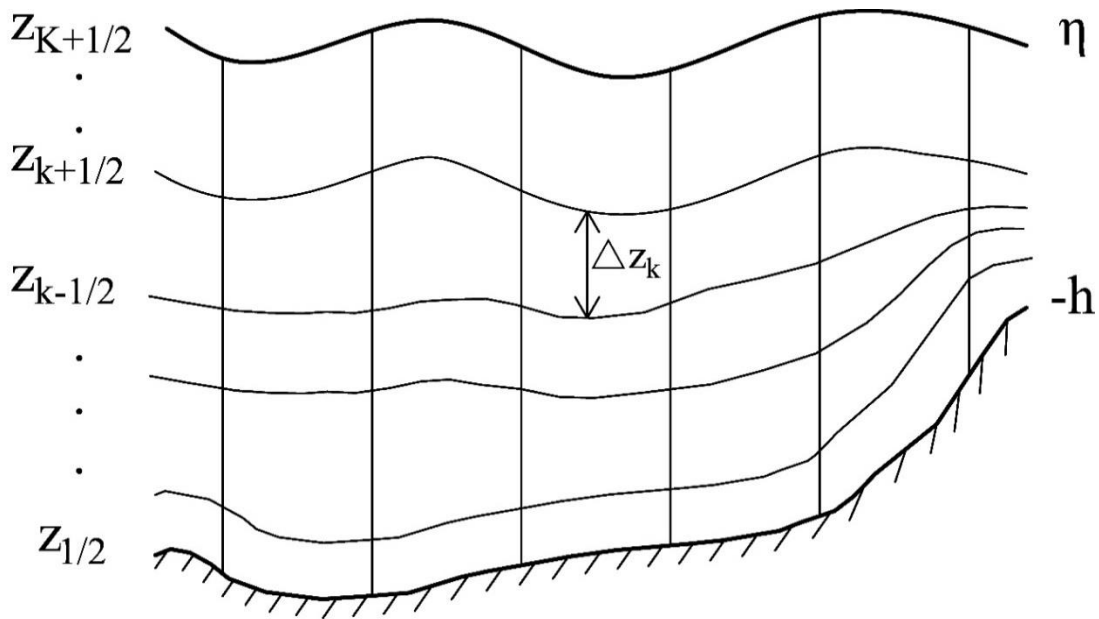


Figure 2. Vertical grid system.

In figure 2, K layers were divided over the vertical direction, and it was defined as

$$z_{k+1/2} = z_{k+1/2}(x, y, t), \quad k = 1, \dots, K \quad (26)$$

where $z_{1/2} = -h(x, y)$ at the bottom, and $z_{K+1/2} = \eta(x, y, t)$ at the free surface.

The vertical velocity relative to layer interface $z_{k+1/2}$ was defined as the difference between the vertical velocity along the streamline and the vertical velocity along the interface as follows

$$\omega_{z_{k\pm 1/2}} = w_{z_{k\pm 1/2}} - \frac{\partial z_{k\pm 1/2}}{\partial t} - u_{z_{k\pm 1/2}} \frac{\partial z_{k\pm 1/2}}{\partial x} - v_{z_{k\pm 1/2}} \frac{\partial z_{k\pm 1/2}}{\partial y} \quad (27)$$

By virtue of the kinematic conditions, it gave

$$\omega_{1/2} = \omega_{K+1/2} = 0 \quad (28)$$

The governing equations were solved by employed the explicit projection method with two steps. Firstly, the momentum equations with the advection and diffusion terms were solved, and the intermediate velocities can be obtained. Secondly, the Pressure Poisson Equation (PPE) which was combined of the discretized continuity and momentum equation were solved, and then the intermediate velocities can be corrected by the pressure term, and the velocities of new step were obtained.

The advection terms and diffusion terms were discretized using the Perot's scheme [31,32]. After the new velocity were achieved, the surface elevation at new step can be calculated by the free-surface equation, and the turbulence flows can also be resolved directly.

The solution process for a step was summarized as follow:

- initializing variables for η , u , v , w , k , ε and p ;
- compute μ_t from equation (9);
- solve discretized momentum equations (2)-(4) to obtain intermediate velocity field $u^{n+1/2}$, $v^{n+1/2}$ and $w^{n+1/2}$ by ignoring the non-hydrostatic term;
- solve the PPE for the non-hydrostatic pressure correction term Δq by substituting the new velocities denoted by the known intermediate velocity field;
- update the non-hydrostatic term and intermediate velocity field to obtain the new velocity field u^{n+1} , v^{n+1} and w^{n+1} ;
- solve the free surface equation (8) to obtain new water level η^{n+1} ;
- compute the vertical grid velocity ω^{n+1} from the semi-discretized form of equation (1);
- solve the k and ε equations (10) and (11).

3. The Blanckaert's experiment and simulation setup

Figure 3 shows a sketch of the sharply curved laboratory flume which made of plexiglas was carried out by Blanckaert at EPFL [33]. The flume consisted of three sections: a 193° bend with constant centerline radius of curvature, $R_c=1.7$ m, was connected with a 9 m long straight channel reach at upstream and followed by a 5 m long outflow section at its downstream. The width of the laboratory flume was $B=1.3$ m and with its vertical sidewalls. The mean flow depth and velocity in the test was $H=0.159$ m and $U=0.43$ m/s, respectively. This gave a Froude number of $F_r=0.34$ (subcritical flow) and a Reynolds number of $R_e=68,400$ (rough turbulent). The bed was filled with a 35 cm thick layer of uniform sand with a median diameter of $d_{50}=2.0$ mm.

The length of the bend section was $L_c=5.73$ m, and the total length of the flume was $L=19.73$ m along the centerline. The experiment was performed in a flume with a relatively shorter ($L_c/B=4.40$) and narrower bend ($B/H=8.18$) with a much stronger curvature ($H/R_c=1/10.69$), as shown in figure 3. Such geometry was rare in natural lowland rivers, but do occur in man-made channel or mountain rivers [34]. Details of the laboratory flume and hydraulic parameters are given in table 1. The detailed 3D measurement results with high spatial and temporal resolution can be founded in Blanckaert [33].

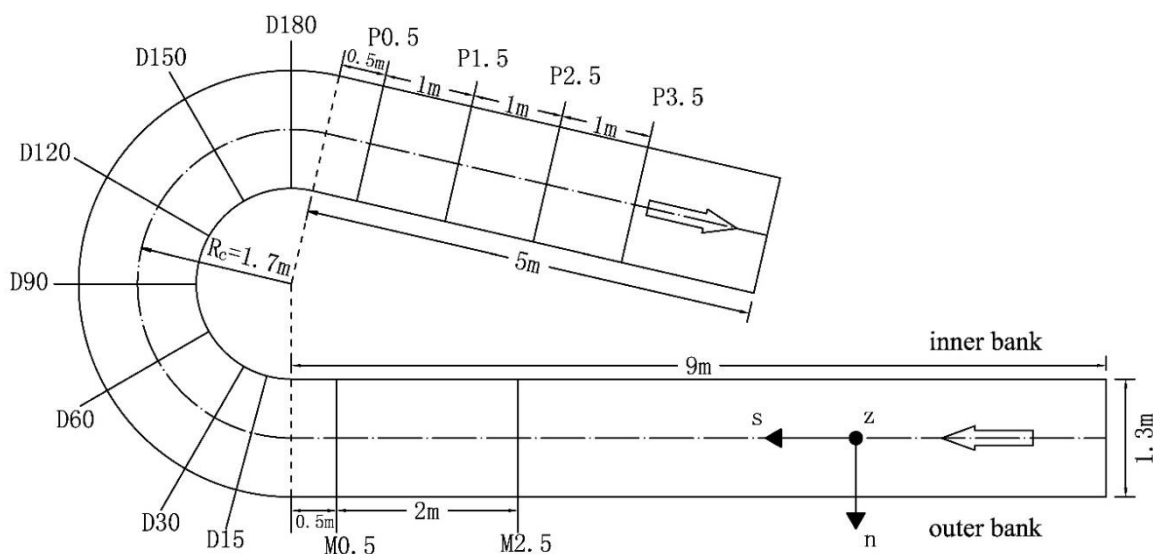


Figure 3. Sketch of the flume in which the 193° bend experiment was performed.

Table 1. Laboratory flume parameters and hydraulic conditions.

	Q	U	H	S	R	u_*	C	d_{50}	R_e	F_r	R_c/B	B/H	H/R_c
unit	[m ³ /s]	[m/s]	[m]	[‰]	[m]	[m/s]	[m ^{1/2} /s]	[mm]	[10 ³]	[-]	[-]	[-]	[-]
Q89	0.089	0.43	0.159	0.94	0.128	0.034	39.6	2.0	68.4	0.34	1.31	8.18	0.094

notes: Q , discharge; $U = Q/(BH)$, flume-averaged velocity; H , flume-averaged water depth; S , flume-averaged water surface gradient on the centerline; R , hydraulic radius; $u_* = \sqrt{gRS}$, shear velocity; $C = (\sqrt{gU})/u_*$, Chezy coefficients; d_{50} , median grain size diameter; $R_e = UH/\nu$, flume-averaged flow Reynolds number; $F_r = U/\sqrt{gH}$, flume-averaged Froude number.

The straight channel reaches were covered by rectangular grids, while the trapezoid grids were used in the bend reach. The simulation replicated the flow condition with 190,920 grid cells (172×37×30) in the longitudinal, transverse and vertical directions, respectively. Sensitivity tests with different vertical grid dimensions indicated that the 30 layers model can represent completely the vertical structure of flow field, particularly close to the bottom. Therefore, 30 uniform vertical layers were specified over the water depth.

The table 1 shows the initial parameters in simulation, and it run until the steady-state was reached. At the upstream entrance, a constant discharge of 0.089 m³/s was specified, while a constant water depth 0.142 m was finally prescribed at the downstream end boundary, which can ensure the depth at the 2.5 m upstream of the bend entrance equals to the value of the experiment. The initial elevation equalled to the value of 0.142 m at the downstream end boundary.

To analyze the influence of non-hydrostatic pressure on the flow pattern in curved channel, the experimental bend has been simulated using both the hydrostatic model and the non-hydrostatic model, and correspondingly, the other parameters remained unchanged.

4. Results and discussion

In the following, the analysis and discussion of the former simulation results are presented from three aspects. The first aspect details the plane distribution and surface profiles of water level at typical cross sections. Then, both the streamwise and transverse velocities profiles over the water depth with the hydrostatic and non-hydrostatic pressure results are illustrated in the second aspect. Finally, the plane distribution of bed shear stress is given in the last aspect.

4.1. Free surface profile

The contour map of water level at the last step was shown in figure 4. The simulation was executed with constant initial and boundary conditions until the steady state solution was reached. It can be seen from the figure 4 that there have no obvious water surface deformation in upstream and downstream straight reaches, and the water level at the inner and outer part of the channel is always consistent. However, once the water flow into the curved reach, severe deformation of water surface is taken place, it shows that the water surface elevation increases at the outer bank and decreases at the inner bank due to the bend curvature and induced secondary current effects. Besides, the water surface gradient close to the inner bank is larger than that of the outer bank, and the free surface deformations disappear rapidly when water flow out of the curved reach.

Figure 5 compares the calculated normalized free surface profiles in some cross sections along the bend with measured data and Zeng's predicted results. In the figure, h_m is the mean water depth in the section, and the horizontal ordinate is given in non-dimensional form as δ/H , with $-B/2 \leq \delta \leq B/2$, where the positive direction is consistent with the transverse direction (n), it towards the outer bank of the channel. The agreement between the calculated free surface profiles and measured data is very good, the magnitude and shape as well as the changing process of the free surface deformations along with the channel bend are well reproduced. The water depth near the inner bank in D30 section is

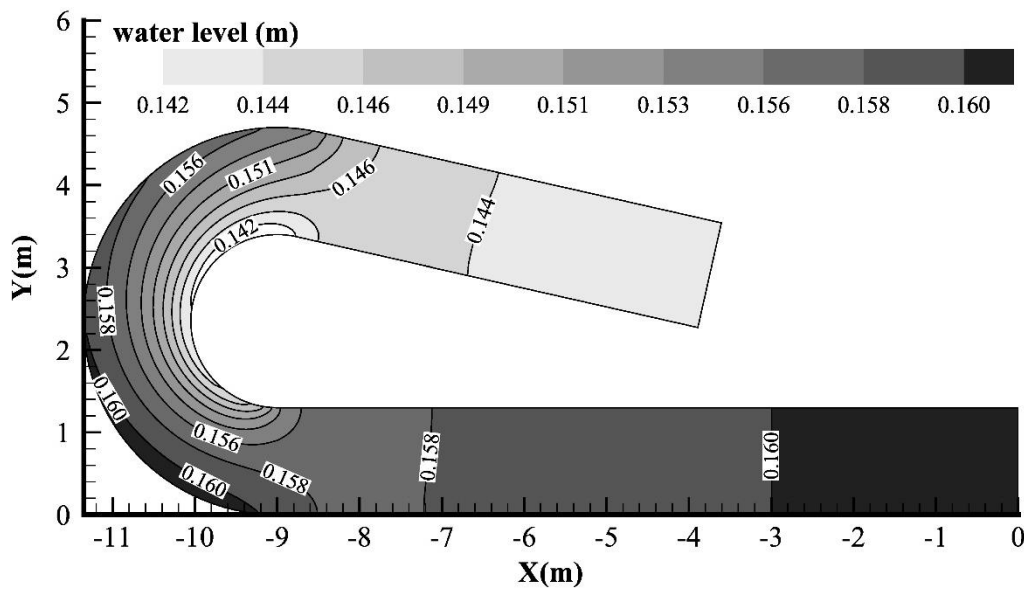
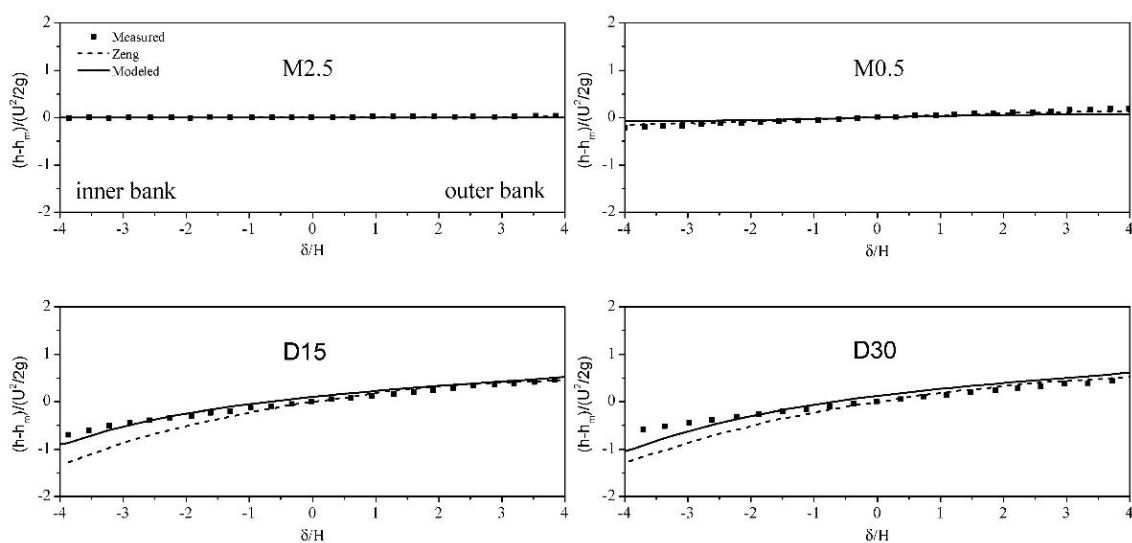


Figure 4. Contour map of water level by numerical calculation.

slightly underpredicted, the root mean square error (RMSE) were 0.24 and 0.16, for the Zeng's results and the simulation results, respectively. The correlation coefficient, which is defined that perfect agreement between the model results and observations yields a value of 1.0, whereas complete disagreement yields a value of 0[35], they were 0.92 and 0.96, respectively. The maximum water level difference between the outer and the inner banks occurs around D90 section in both experiment and simulation, it was also well reproduced, the RMSE were 0.09 and 0.08, and the correlation coefficient were 0.99 and 0.99 respectively. For other sections, the RMSE were 0.23 and 0.09, and the correlation coefficient were 0.93 and 0.99 in D15 section, correspondingly, 0.13 and 0.09 for RMSE, and 0.97 and 0.99 for correlation coefficient in D180 section. In the P0.5 section, poor agreement appeared with RMSE of 0.04 and 0.15, and correlation coefficient of 0.99 and 0.90, respectively. In general, the present simulation with height function method to trace free surface motion is capable of predicting a better water level deformation in sharply curved channel. Moreover, the hydrostatic pressure difference induced by superelevation is the main factor affecting the formation of transverse circulation.



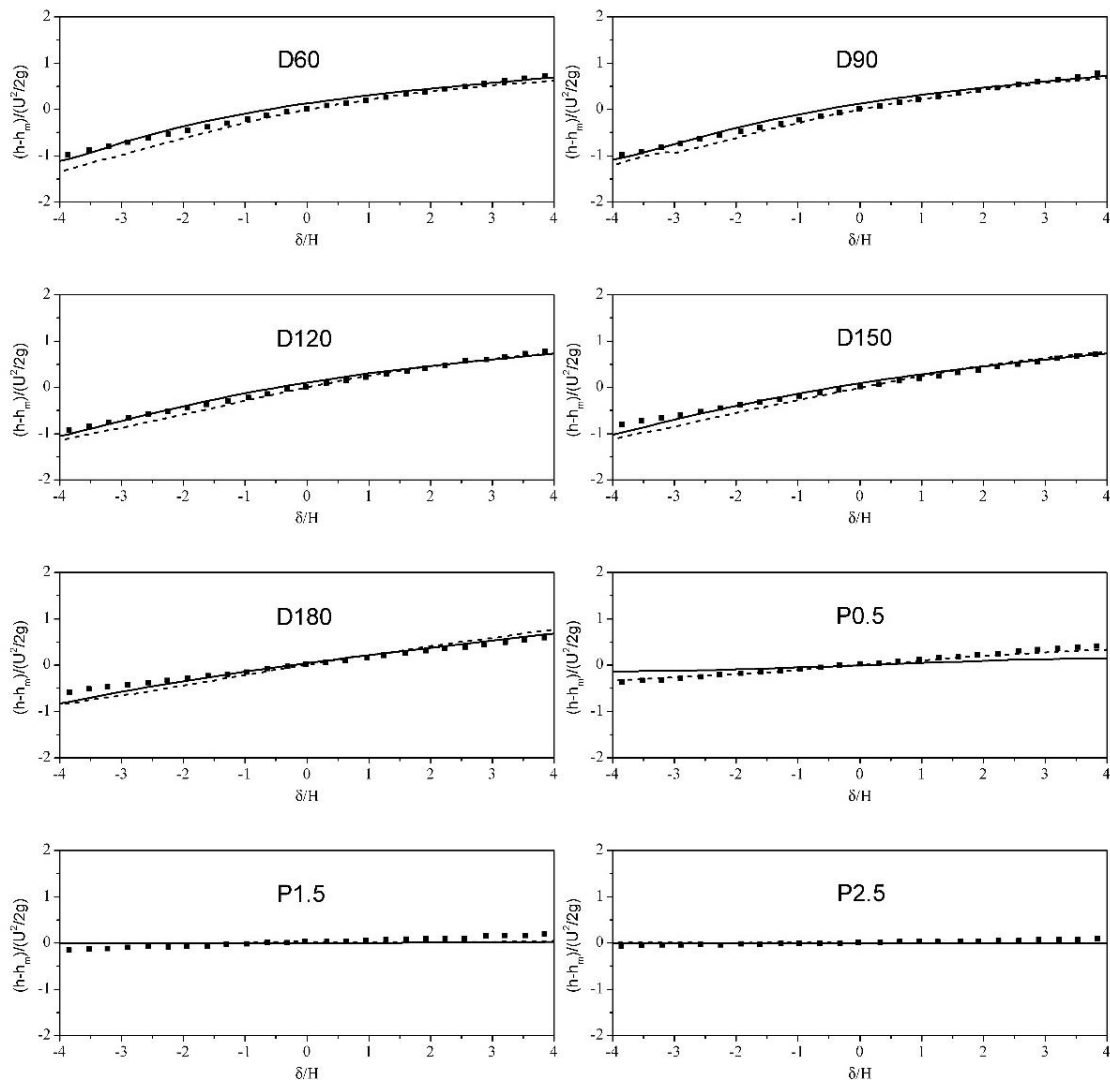
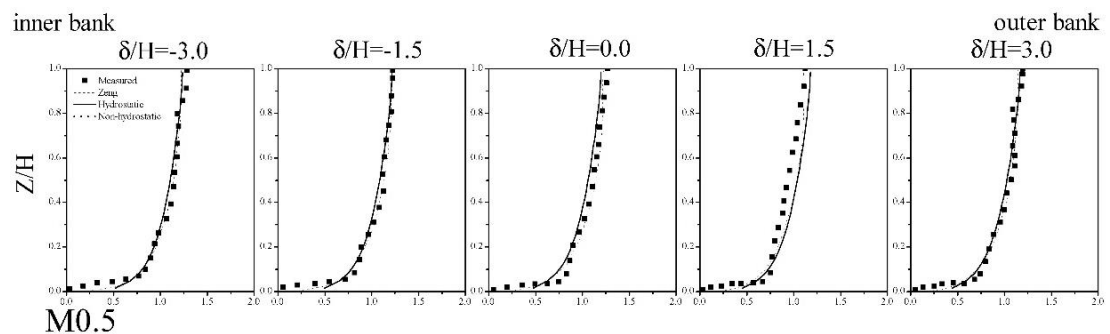


Figure 5. Comparison of normalized free surface profiles between measured (symbols) and computed (Zeng’s (dashed lines) and this article (solid lines)) in typical cross sections along the channel bend.

4.2. Flow field

The profiles of streamwise velocity in cross-sections along the bend are compared in figure 6. The velocity and depth are correspondingly represented by horizontal and vertical axis. And they are normalized with the bulk channel velocity and local water depth, respectively. In the figure, six typical sections along the bend are selected, and five points in plane are located in each section.



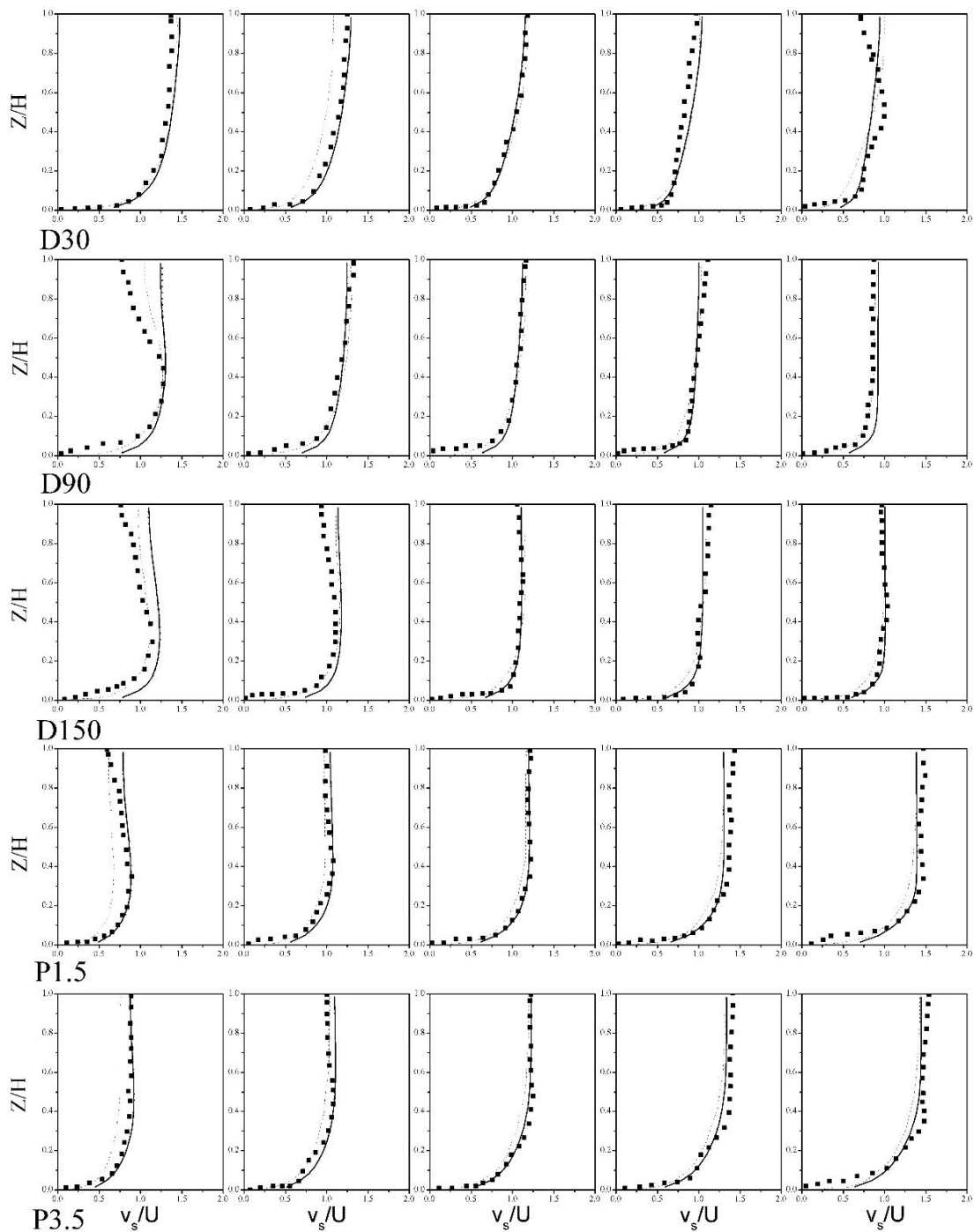


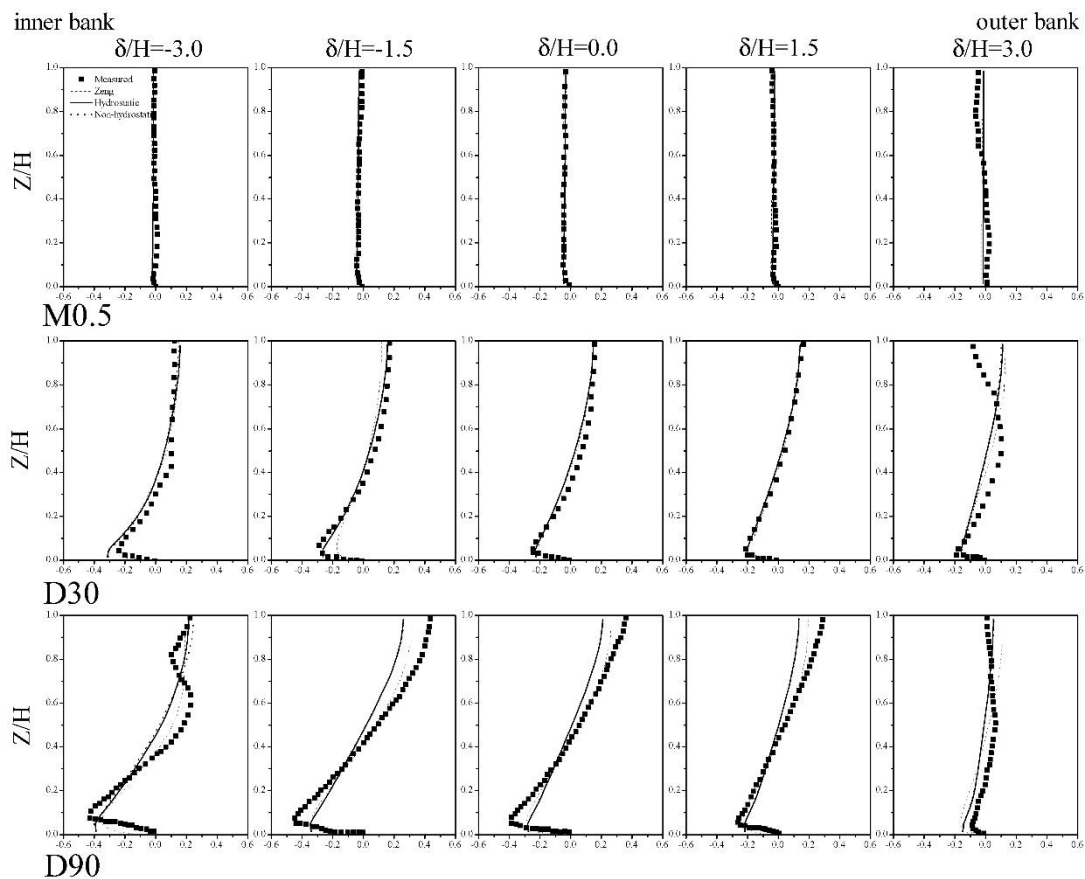
Figure 6. Comparison of vertical profiles of streamwise velocity between measured (symbols) and computed (Zeng’s (dashed lines) and this article with hydrostatic (solid lines) and non-hydrostatic (dot lines)) in typical cross sections along the channel bend.

Overall, the simulations capture the main features of flow structure over water depth in the bend. The vertical profiles of the streamwise velocity behave typical logarithmic distribution in section M0.5 as the fully developed flow in the upstream straight reach, and there have no noticeable difference in the whole cross section. In section D30, the magnitudes of the velocity close to the inner bank increase while those near the opposite bank decrease once the water flows into the curved reach. The RMSE at

points $\delta/H = -1.5$ were 0.15, 0.09 and 0.09 for the Zeng's results and hydrostatic and non-hydrostatic results, and the correlation coefficient were 0.89, 0.96 and 0.96, respectively. In section D90 and D150, the velocities at points $\delta/H = -3.0$ have pronounced variations, and the maximum velocity in vertical direction moves from the free surface down to the lower part of the water column. Although the simulations correctly predict the maximum velocity in section D90, the velocities at free surface in D90 and the full vertical profile in D150 are overpredicted. The RMSE at midpoints $\delta/H = 0.0$ in section D150 were 0.08, 0.11 and 0.11, and the correlation coefficient were 0.96, 0.92 and 0.92, respectively. Besides, the vertical profiles of streamwise velocities are no longer logarithmic distribution, they are flattened by increasing the velocities in the lower part of the water column and decreasing the velocities in the free surface part. Which are consistent to the observation by De Vriend [4], and this reduces the intensity of the centrifugal force effects and in turn weakens the intensity of the main recirculation eddy [1]. In the downstream part of the channel, the velocities close to the inner bank decrease continually and that near the opposite bank increase correspondingly in section P1.5 and P3.5. And the distributions of velocity profiles are gradually recovered from flattening to log-type again as the water flows away from the curved reach. The average RMSE in section P1.5 were 0.11, 0.11 and 0.11, and the average correlation coefficient were 0.91, 0.90 and 0.90, respectively.

Throughout all the selected sections along the channel, the maximum streamwise velocities are close to the inner bank at the entrance of the curved reach at the beginning, and then they gently shift toward the outer bank along with the water flow movement, near the exit of the curved reach the maximum streamwise velocities are close to the outer bank and they keep this pattern for some distance in the downstream reach. This process can be regarded as the trace of main flow.

Figure 7 shows the comparison of vertical profiles of transverse velocities between measured and calculated in typical sections along the bend. It has the same sections and non-dimensional treatment manners to the figure 6.



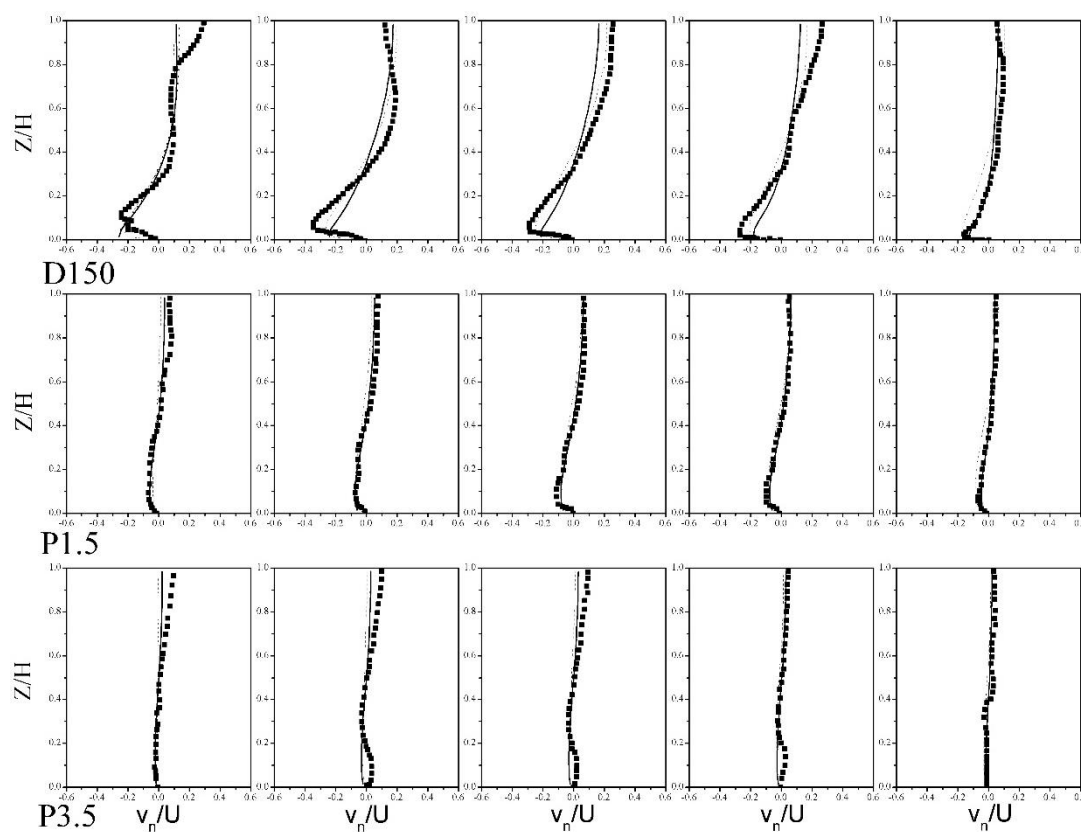


Figure 7. Comparison of vertical profiles of transverse velocity between measured (symbols) and computed (Zeng's (dashed lines) and this article with hydrostatic (solid lines) and non-hydrostatic (dot lines)) in typical cross sections along the channel bend.

In general, compared to the magnitudes of velocities in streamwise directions, those in transverse direction are much smaller. The predictions in straight reach and upstream bend are better than that of downstream bend, even though the predictions can capture the features of vertical profiles in sections D90 and D150, and the disagreements mainly occurs at the magnitudes of the velocities. In the upstream and downstream straight reach, the transverse velocities are fairly weak except for the section P1.5, which is still much effected by secondary circulation because of the close to the upstream curved reach. The predictions show excellent agreement with the measurements in section D30, except for the point at $\delta/H=3.0$ where the transverse velocity becomes negative near the free surface, The average RMSE in this section were 0.05, 0.05 and 0.05, and the average correlation coefficient were 0.92, 0.91 and 0.92, respectively. Maybe there present the backward secondary outer-cell close to the outer bank in experiment observations, however, this phenomenon was not captured by the simulations as well as Zeng's. The reason may be related to the nonlinear turbulence model which can account for non-isotropic turbulence effects, as the reason that the outer-bank circulation is generated by the anisotropy of the cross-stream turbulence [13]. The same situation can also be found at the same point in section D90. The section D90 is located near the apex of the bend, where the secondary flow is fully developed. The intensity of the secondary circulation increases sharply in section D90, particularly close to the inner bank. Unfortunately, the simulations generally underpredict the maximum transverse currents both in the top and bottom of the water column with adverse directions. The average RMSE in this section were 0.06, 0.10 and 0.10, and the average correlation coefficient were 0.92, 0.88 and 0.88, respectively. Notwithstanding the intensities of transverse current in section D150 decrease evidently, the underprediction still present in most points of the section. The average RMSE in this section were 0.06, 0.07 and 0.07, and the average correlation coefficient were 0.94, 0.92

and 0.92, respectively. The prediction close to the outer bank has acceptable agreements with measurements along with the disappearance of the outer-bank cell. The simulation results display a fast decay of transverse velocity at downstream straight reach, and the simulations have good agreements with observations.

The hydrostatic pressure and non-hydrostatic pressure results are also presented in figure 6 and figure 7. The differences between the two sub-model results are negligible, and the non-hydrostatic pressure model does not display its performance in this sharp channel bend. However, the non-hydrostatic model has showed its significant benefits in short wave problems [24,25], and it has hardly any influence on the flow pattern in sharp channel bends. The reason maybe the vertical acceleration in the channel bends is not dramatic, particularly for steady flow in channels as the non-hydrostatic model is based on the hypothesis that the hydrodynamic pressure can not be neglected when there has intensive vertical acceleration.

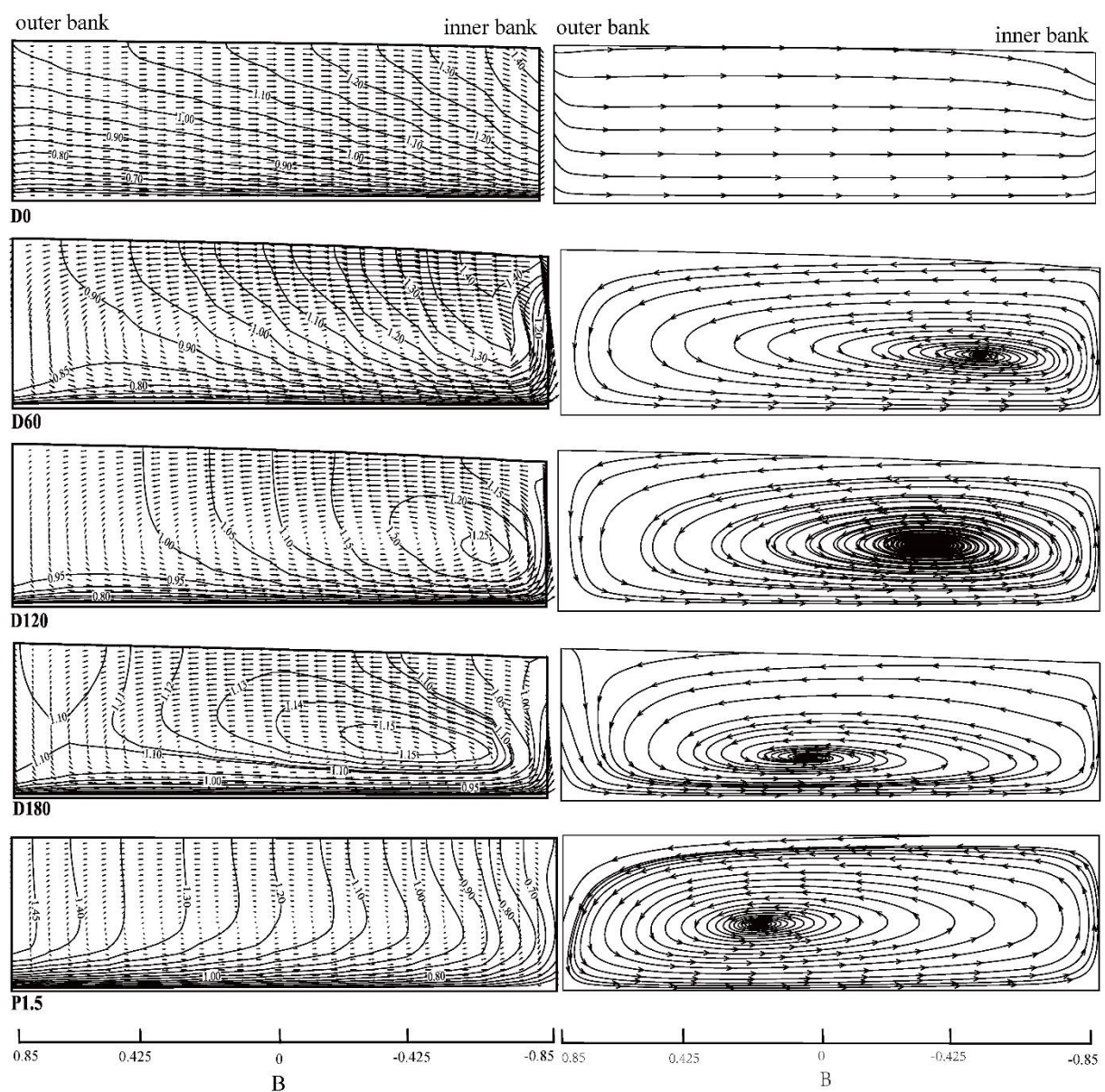


Figure 8. Contour maps of streamwise velocities and transverse secondary circulations (left), as well as streamline patterns (right) in typical cross section along the channel bend.

Figure 8 show the contour map of streamwise velocities and transverse secondary circulations, as well as streamline patterns in typical sections along the bend. It can be distinguished easily the inner and outer banks from the free surface shape in figure 8. And from the contour map of streamwise velocities in the left side of figure 8, it can be seen that the maximum velocities in vertical direction display process shifting from the free surface to close to the bottom of the water column, simultaneously, they shift from close to the inner bank at the entrance (section D0) toward near the opposite bank at the exit and downstream straight reach (sections D180 and P1.5) in the transverse direction.

It also can be seen from the transverse velocity field in the left side of figure 8 that the transverse velocities began to appear and all move toward the inner side at the entrance of the bend, as the bend turn right the fluid are forced to make adjustment. In the following curved reach in sections D60, D120 and D180, as a consequence of the actions of the centrifugal forces and water pressures which results in the transverse circulation, it shows that the current moves toward the outer bank close to the free surface and toward the inner bank close to the bottom, remarkably, due to the restrict of vertical wall boundaries, the upward current and downward current occur near the inner and outer bank, respectively. Under the action of inertia forces, the transverse circulation still present as the flow past the curved reach in section P1.5, but the strength of transverse circulation is much smaller than that of upstream curved reach.

From the streamline patterns on the right side of figure 8, it can be seen that the core of the transverse eddy cell in transverse direction moves away from the side close to the inner side and toward the opposite side close to the outer side (from section D60 to section P1.5), simultaneously, they shift from near the middle of the water column downward close to the bottom (from section D60 to section D180) and then move upward again in the downstream straight reach (in section P1.5) in vertical direction as the intensity of the secondary flow is decaying and the flow pattern is gradually recovering fully developed turbulent flow in straight channel.

4.3. Bed shear stress

Figure 9 shows the contour map of normalized bed shear stress by numerical calculation. The bed shear stress represents the stream intensity near the river bed, and it will help to determine the initial erosion/deposition process in alluvial channels. For in sharply curved channel due to the presence of highly three-dimensional flow features, the accurate simulation of bottom velocity field as well as bed shear stress by three-dimensional model can provide guarantee for the subsequent bed deformation calculation.

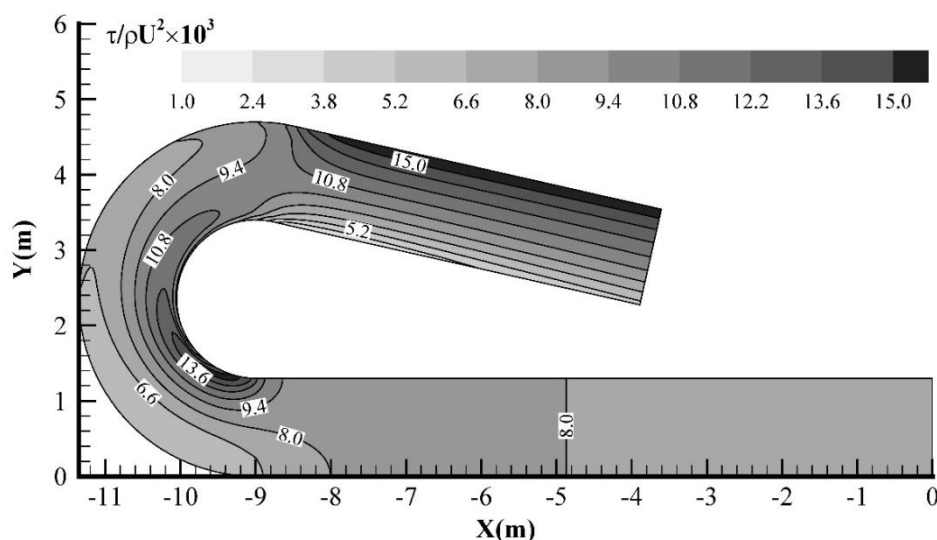


Figure 9. Contour map of normalized bed shear stress by numerical calculation.

The bed shear stress in the upstream straight reach keeps uniform distribution across the whole section, but this uniform stage is broken in the following curved and downstream straight reaches. The bed shear stress is moderately amplified near the inner bank around section D30 and is strongly amplified near the outer bank once enter into the downstream straight reach. There have apparent differences between inner and outer banks. Although the region close to the inner bank in curved channel has relatively large bed shear stress, it often takes place deposition due to the sediment particles are transported from the outer bank to the inner bank by the bottom current.

The amplification close to the outer bank in outlet straight reach is nearly twice times than that of fully developed flow in upstream incoming straight reach. The results are consistent with preceding analysis on streamwise velocities, and the magnitude and location of bed shear stress also vary along with the route of the main flow.

5. Conclusions

A three-dimensional numerical model with hydrostatic pressure and non-hydrostatic pressure sub-models has been developed to calculate the flow field and bed shear stress in a laboratory flume experiment of Blanckaert [32] which features a sharp open channel bend with 193° curved reach. The model predictions were verified with the experimental results obtained by Blanckaert. The comparisons of the predicted and measured data showed that the predictions were capable of capturing the main bend flow features. The verification of free surface profile showed that the three-dimensional numerical model with height function method can track the free surface motion efficiently and correctly in sharp channel bends. And it has advantages for dealing with similar problems with significant water level difference and large scale natural river bends. The simulation reproduces the three-dimensional flow characteristics in sharp open channel bends after verification of velocity profile over depth in streamwise and transverse directions respectively. It can be found from the study results that the distributions of velocity profiles vary from log-type to flattening and recover to logarithmic distribution again along with the water flow moving. The changes of maximum velocity in a section and across sections display the shift route of main flow, it shift from the inner bank toward the outer bank and keep close to the outer bank for some distance at the exit of the curved reach and past it. The comparison between hydrostatic model and non-hydrostatic model showed that non-hydrostatic model has no noticeable influence on flow pattern in this sharp channel bend with highly three-dimensional flow characteristics.

Acknowledgments

This research work is funded by the National Natural Science Foundation of China (Grant No. 51609010), and the Central Fundamental Research Funds for the TIWTE (Grant No. TKS170220, TKS170222, TKS170216).

References

- [1] Zeng J 2006 Fully 3D non-hydrostatic model to compute flow, sediment transport and bed morphology changes for alluvial open channel bends (Iowa, Iowa City: The University of Iowa)
- [2] Blanckaert K 2009 Saturation of curvature-induced secondary flow, energy losses, and turbulence in sharp open channel bends: laboratory experiments, analysis, and modeling *J. Geophys. Res.* **114** F03015
- [3] Onishi Y 1972 Effects of meandering of sediment discharges and friction factors of alluvial streams (Iowa, Iowa City: The University of Iowa)
- [4] De Vriend H J 1981 Velocity redistribution in curved rectangle channels *J. Fluid. Mech.* **107** 423-39
- [5] Struiksma N, Olesen K W, Flokstra C and de Vriend H J 1985 Bed deformation in curved alluvial channels *J. Hydraul. Res.* **23** 57-79
- [6] Steffler P, Rajaratnam N and Peterson A 1985 LDA measurements in open channel *J. Hydraul.*

- Eng.* 10.1061/(ASCE)0733-9429(1985)111:1(119)
- [7] Olesen K W 1985 Experiments with graded sediment in the DHL curved flume *Report R 657-XXII M1771* (The Netherlands, Delft: Delft Hydraulic Laboratory)
- [8] Odgaard A J and Bergs M A 1988 Flow processes in a curved alluvial channel *Water Resour. Res.* **24** 45-56
- [9] Blanckaert K and De Vriend H J 2010 Meander dynamics: a nonlinear model without curvature restrictions for flow in open-channel bends *J. Geophys. Res.* **115** F04011
- [10] Shimizu Y and Itakura T 1989 Calculation of bed variation in alluvial channels *J. Hydraul. Div.* **115** 367-84
- [11] Kassem A A and Chaudhry M H 2002 Numerical modeling of bed evolution in channel bends *J. Hydraul. Eng.* 10.1061/(ASCE)0733-9429(2002)128:5(507)
- [12] Wu W M 2004 Depth-averaged 2-D numerical modeling of unsteady flow and nonuniform sediment transport in open channels *J. Hydraul. Eng.* **130** 1013-24
- [13] Blanckaert K and Graf W H 2004 Momentum transport in sharp open-channel bends *J. Hydraul. Eng.* 130 10.1061/(ASCE)0733-9429(2004)130:3(186)
- [14] Ghamry H K and Steffler P M 2005 Two-dimensional depth-averaged modeling of flow in curved open channels *J. Hydraul. Res.* **43** 44-55
- [15] Choi S U, Kim T B and Min K D 2005 2D Finite element modeling of bed elevation change in a curved channel *River Proceedings of the 4th IAHR Symposium on River, Coastal and Estuarine Morphodynamics* (Urbana, Illinois)
- [16] Vasquez J A, Steffler P M and Millar R G 2005 River2D morphology, Part II: curved alluvial channels *17th Canadian Hydrotechnical Conference on Hydrotechnical Engineering* (Edmonton, Alberta)
- [17] Wu W M, Rodi W and Wenka T 2000 3D numerical modeling of flow and sediment transport in open channels *J. Hydraul. Eng.* **126** 4-15
- [18] Lesser G R, Roelvink J A, van Kester J A T M and Stelling G S 2004 Development and validation of a three-dimensional morphological model *Coast. Eng.* **51** 883-915
- [19] Rüther N and Olsen N R B 2005 Three-dimensional modeling of sediment transport in a narrow 90° channel bend *J. Hydraul. Eng.* 10.1061/(ASCE)0733-9429(2005)131:10(917)
- [20] Khosronejad A, Rennie C D, Salehi Neyshabouri A A and Townsend R D 2007 3D numerical modeling of flow and sediment transport in laboratory channel bends *J. Hydraul. Eng.* **133** 10.1061/(ASCE)0733-9429(2007)133:10(1123)
- [21] Zeng J, Constantinescu G, Blanckaert K and Weber L 2008 Flow and bathymetry in sharp open-channel bends: experiments and predictions *Water Resour. Res.* **44** W09401
- [22] Kashyap S, Constantinescu G, Rennie C D and Post G 2012 Influence of channel aspect ratio and curvature on flow, secondary circulation and bed shear stress in a rectangular channel bend *J. Hydraul. Eng.* **138** 1045-59
- [23] Zeng J, Constantinescu G and Weber L 2008 A 3D non-hydrostatic model to predict flow and sediment transport in loose-bed channel bends *J. Hydraul. Res.* **46** 356-72
- [24] Ai C F, Jin S and Lv B 2010 A new fully non-hydrostatic 3D free surface flow model for water wave motions *Int. J. Numer. Meth. Fluids.* **66** 1354-70
- [25] Ai C F and Jin S 2012 A multi-layer non-hydrostatic model for wave breaking and run-up *Coast. Eng.* **62** 1-8
- [26] Xing Y 2014 Study and application of three-dimensional numerical modeling of bed deformation in curved channel and salinity transport in estuary (China: Dalian University of Technology)
- [27] Ransau S R 2002 Solution methods for incompressible viscous free surface flows: a literature review *Report* (Trondheim, Norway: Department of Mathematical Sciences, Norwegian University of Science and Technology)
- [28] Stansby P K and Zhou J G 1998 Shallow-water flow solver with non-hydrostatic pressure: 2D vertical plane problems *Int. J. Numer. Meth. Fluids.* **28** 541-63

- [29] Zijlema M and Stelling G S 2005 Further experiences with computing non-hydrostatic free-surface flows involving water waves *Int. J. Numer. Meth. Fluids.* **48** 169-97
- [30] Ai C F and Jin S 2010 Non-hydrostatic finite volume model for non-linear waves interacting with structures *Computers & Fluids.* **39** 2090-100
- [31] Perot B 2000 Conservation properties of unstructured staggered mesh schemes *Journal of Computational Physics* **28** 541-63
- [32] Kramer S C and Stelling G S 2008 A conservative unstructured scheme for rapidly varied flows *Int. J. Numer. Meth. Fluids.* **58** 183-212
- [33] Blanckaert K 2002 Flow and turbulence in sharp open-channel bends (Switzerland: École Polytechnique Fédérale de Lausanne)
- [34] Blanckaert K and de Vriend H J 2005 Turbulence characteristics in sharp open-channel bends *Phys. Fluids.* **17** 055102
- [35] Xing Y, Ai C F and Jin S 2013 A three-dimensional hydrodynamic and salinity transport model of estuarine circulation with an application to a macrotidal estuary *Appl Ocean Res.* **39** 53-71